Synthetic satellite imagery for current and future environmental satellites

Lewis D. Grasso [a]; Manajit Sengupta [a]; John F. Dostalek [a]; Renate Brummer [a]; Mark Demaria [b]

[a] Cooperative Institute for Research in the Atmosphere (CIRA)/Colorado State University, Fort Collins, CO 80523-1375, USA [b] NOAA/NESDIS/STAR/RAMMB, Fort Collins, CO, USA

First Published:2008

PLEASE SCROLL DOWN FOR ARTICLE

Synthetic satellite imagery for current and future environmental satellites

LEWIS D. GRASSO*†, MANAJIT SENGUPTA†, JOHN F. DOSTALEK†,
RENATE BRUMMER† and MARK DEMARIA‡

†Cooperative Institute for Research in the Atmosphere (CIRA)/Colorado State
University, 1375 Campus Delivery, Fort Collins, CO 80523-1375, USA
‡NOAA/NESDIS/STAR/RAMMB, Fort Collins, CO, USA

During the next decade, data from a new generation of US geostationary and
polar orbiting satellites will become available. To prepare for these data,
representative imagery of these satellites is desirable. Two independent methods
have been developed to create imagery from future satellites before they are
placed into orbit. One method uses data from current operational and
experimental satellites. Data obtained this way are referred to as simulated
imagery. Another method generates satellite imagery by using numerical models.
Data obtained by this method are referred to as synthetic imagery. Each method
has some weaknesses that can be overcome by using both methods together.
Synthetic imagery for two future US sensors is introduced in this paper.
Emphasis is placed on a severe thunderstorm event.

1. Introduction

Images approximating those that will be received from future satellite instrumenta-
tion can be generated in two independent ways. One way is to use data from existing
operational and/or research satellites. For example, Li *et al.* (2004) demonstrated the
combined use of Moderate Resolution Imaging Spectroradiometer (MODIS) and
Atmospheric Infrared Sounder (AIRS) data. They further pointed out that their
procedure is relevant to the use of future data from the Geostationary Operational
Environmental Satellite R (GOES-R). Hillger and Clark (2002) describe principal
component analysis of satellite data and suggest implications to future GOES-R
data. A second way relies on numerical models. A weather prediction model is used
to simulate a weather event and its output is used in a second model that generates
synthetic satellite images. Chaboureau and Pinty (2006) used this technique to
validate a cirrus parameterization scheme. Raymond and Aune (2003) produce
synthetic water vapour imagery from the Cooperative Institute for Meteorological
Satellite Studies (CIMSS) Regional Assimilation System (CRAS) model. Morcrette
(1991) used this procedure to validate cloud fields produced by the European Centre
for Medium-Range Weather Forecasts (ECMWF). Images created by the first
method will be called simulated images, while images created by the second method
will be called synthetic images. Both methods are currently being used to prepare for
the next generation of operational US National Oceanic and Atmospheric

---

*Corresponding author. Email: grasso@cira.colostate.edu

Administration (NOAA) geostationary and polar-orbiting satellites: the GOES-R and the National Polar-Orbiting Operational Environmental Satellite System (NPOESS). These techniques, however, apply just as well to any other international environmental satellite sensor; for example, the European Meteosat Series, the Geostationary Meteorological Satellite programme in Japan, and the Indian National Satellite System.

Data from the MODIS (King *et al.* 1992) and the AIRS (Aumann *et al.* 2003) have been used as a first step to simulate future GOES-R Advanced Baseline Imager (ABI) images (Schmit *et al.* 2005). These instruments collect data near wavelengths that are planned for the ABI. Further details and a comprehensive discussion of the GOES-R ABI can be found in Schmit *et al.* (2005). Similarly, images for the future NPOESS Visible/Infrared Imager/Radiometer Suite (VIIRS) can also be obtained from current satellites. For example, the Defense Meteorological Satellite Program Operational Linescan System, the Polar Orbiting Environmental Satellite (POES) Advanced Very High Resolution Radiometer (AVHRR), and MODIS imagery can be used to simulate VIIRS data (Miller *et al.* 2006). Further details on the NPOESS VIIRS can be found in Miller *et al.* (2006).

Future sensors are likely to have spatial resolutions and sampling rates that exceed those onboard current satellites. This can create a problem when producing simulated images. Simulated GOES-R ABI images derived from current instruments illustrate this issue. In the infrared ranges, the instantaneous geometric field of view (IGFOV) at the nadir of the ABI sensor on GOES-R will be about 2 km. In addition, temporal sampling of 5 min is planned (Schmit *et al.* 2005). Instruments aboard current polar-orbiting satellites can simulate a 2-km ABI image, although simulated data from a polar-orbiting satellite cannot match the 5-min temporal sampling. This is because a polar-orbiting satellite passes over a given midlatitude area only twice per day. However, the current GOES can produce a sequence of infrared images at a 5-min sampling rate, but cannot match the planned 2-km IGFOV on the ABI with their 4-km IGFOV.

The aim of this paper was to introduce synthetic GOES-R ABI and NPOESS VIIRS satellite imagery. These images serve to complement simulated GOES-R ABI and NPOESS VIIRS imagery from existing operational and research satellites. The procedure for generating synthetic satellite imagery was developed at the Cooperative Institute for Research in the Atmosphere (CIRA) over the past few years. Besides Chevallier and Kelly (2002) and Chevallier *et al.* (2001), a dearth of information exists in the peer-reviewed literature on the development of synthetic satellite images from model data, especially imagery that contains clouds. Imagery presented in this paper is the first attempt at producing synthetic imagery of future satellites from model outputs. As mentioned earlier, the emphasis is on the generation of synthetic satellite imagery. A certain degree of inaccuracy in the output of a numerical model is acceptable because such discrepancies have no effect on the procedure to generate synthetic imagery.

The Regional Atmospheric Modeling System (RAMS; Cotton *et al.* 2003), with two-way interactive nested grid capabilities and a two-moment microphysical scheme, is used in conjunction with an observational operator to create synthetic satellite imagery. This method was first applied to the 2 May 1996 stratus cloud over Texas and Oklahoma in the USA (Greenwald *et al.* 2002). This system was extended by Grasso and Greenwald (2004) and applied to an idealized thunderstorm. Details of RAMS and the observational operator can be found in Greenwald *et al.* (2002)

and Grasso and Greenwald (2004). A first step at validating this procedure is discussed by, and applied to, the results of Greenwald *et al.* (2002). In the present work, synthetic GOES-R ABI imagery at 10.35 μm and synthetic NPOESS VIIRS imagery at 11.02 μm are presented for the 8 May 2003 severe weather outbreak over the Central Plains of the USA. Synthetic GOES-12 imagery at 10.7 μm is also shown for a comparison between future and current sensors.

This paper is divided into seven sections. An overview of the case study is presented in section 2. The model set-up and initialization is discussed in section 3 and synthetic imagery is presented in section 4. A discussion of the usefulness of synthetic imagery along with additional motivation to generate such imagery is presented in section 5. A brief discussion of future work is presented in section 6 followed by a summary in section 7.

2. 8 May 2003 case study

Because of the proposed temporal and spatial sampling of the ABI on GOES-R, the 8 May 2003 severe weather event was chosen as the case study. This event includes rapidly evolving convection that would require relatively high temporal sampling to capture. At 500 hPa, a jet streak developed over the region by the afternoon with an embedded southwesterly flow just under $40 \, \mathrm{m \, s^{-1}}$ (88 kts), as depicted in figure 1(*a*). Thunderstorms developed along the dryline in the afternoon, moved eastwards, and produced high surface winds, hail and tornadoes. Reports of 54 tornadoes, 71 occurrences of wind damage, and 188 large hail observations were a result of this severe weather event. An afternoon GOES-12 visible image of the event is shown in figure 1(*b*). In addition, a region of low pressure was positioned over western Nebraska. A warm front extended eastwards along the border of Nebraska and Kansas. Further south, a dryline developed over central Kansas that extended from the warm front southwards into Oklahoma. Morning surface temperatures, just east of the dryline, increased to near 301 K (28°C, 82°F) during the afternoon while surface dewpoint temperatures were near 295 K (22°C, 72°F). Surface winds veered from a southerly direction, east of the dryline, to a southwesterly direction, west of the dryline. Surface wind speeds gusted to $20 \, \mathrm{m \, s^{-1}}$ (44 kts) west of the dryline; as a result, blowing dust was observed over western and central Kansas. Thunderstorms that developed along the dryline are the focus of this simulation.

3. Computational methodology

A total of four grids were used in this simulation. Horizontal grid spacings, in both directions, of 50 km, 10 km, 2 km, and 400 m in grids 1–4, respectively, were used. The horizontal grid spacing in grid 3 was chosen to be 2 km because this value is near the horizontal footprint of the GOES-R ABI. Similarly, the horizontal grid spacing of 400 m in grid 4 is approximately the horizontal footprint of the VIIRS instrument. Ideally, a fifth grid would be used to fully resolve features in grid 4 with a 400 m length scale. Because of memory limitation, however, grid 5 was not possible. Grid 1 had 90×66 points, grid 2 had 192×162, grid 3 had 502×522, and grid 4 had 852×1027 grid points in the *x* and *y* directions. All grids had 60 vertical levels. The vertical grid spacing was stretched from 100 m near the surface to 500 m near the height of 4.5 km and was kept fixed at 500 m up to the top of the simulated domain that was near 24 km. This choice of vertical grid spacing was motivated by two factors. First, the relatively small vertical grid spacings in the boundary layer
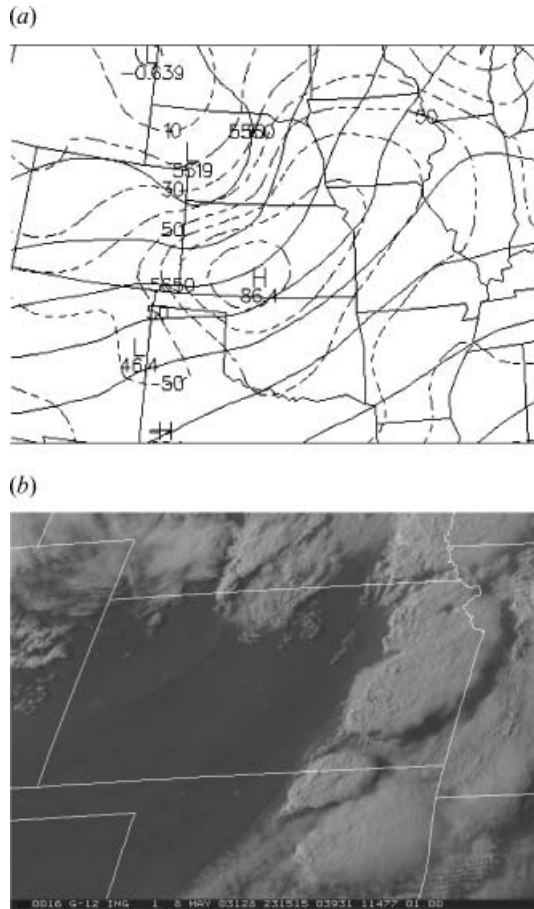
Figure 1. (*a*) 500 hPa geopotential heights (solid lines, every 45 m) and wind speeds (broken lines, every 10 kts) for 0000 UTC 9 May 2003 (courtesy of Plymouth State Weather Center) and (*b*) 1.0 km GOES-12 visible image at 2315 UTC on 8 May 2003.

will aid in resolving processes that allow lifting of air into the convective updrafts. Second, 500 m vertical grid spacing at anvil level was desirable to resolve the thickness of the anvils of the thunderstorms. This value, however, may be too large; that is, 500 m vertical grid spacing may be too large to resolve thin cirrus. Because of computer memory limitations, smaller vertical grid spacings near the anvil level were not possible. As a result of the grid configurations, grid 1 covered most of the USA, grids 2 and 3 covered most of the central plains while grid 4 covered east central Kansas (figure 2).

Grids 1–3 were initialized from the National Center for Environmental Prediction (NCEP) NAM model (formerly Eta) analysis data. Grid 4 was spawned during the simulation and thus was initialized from grid 3. The simulation was started at 1200 UTC 8 May 2003. At 1800 UTC, grid 4 was spawned over east central Kansas, prior to the development of thunderstorms in that region. Ideally, grid 4 should have been initialized at 1200 UTC along with the other three grids. However, in an attempt to complete the simulation in a reasonable time, grid 4 was spawned during the simulation. At 0000 UTC, the simulation was terminated. As a result, grid 4 was active for 6 h. Horizontally varying soil moisture was included in all four grids.
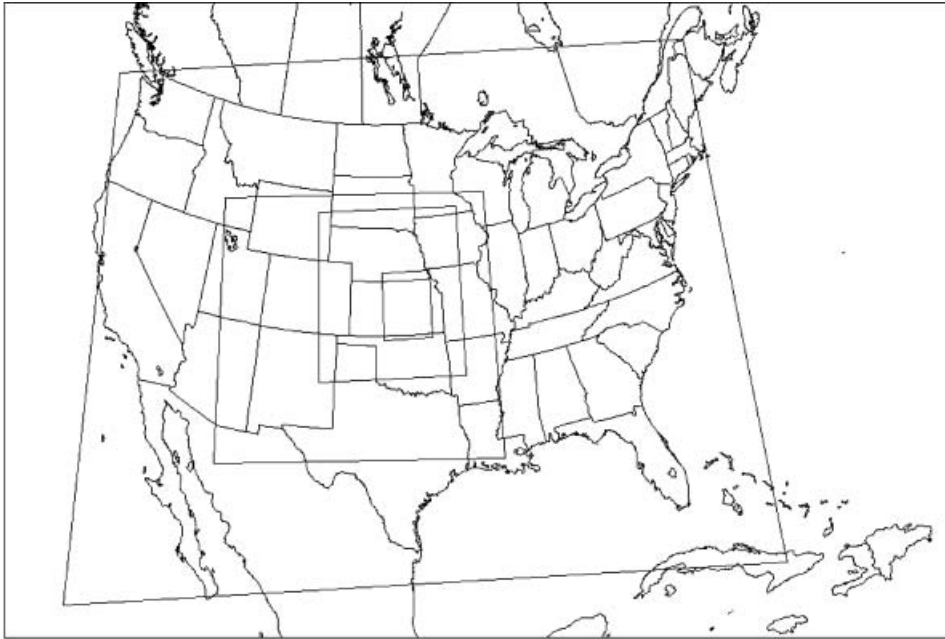
McIDAS

Figure 2. Map of the USA along with boundaries of grids 1–4 that were used for the 8 May 2003 severe weather simulation.

A 64-bit Linux cluster was used to run this simulation. With four grids active, approximately 25 GB of memory were allocated during the run. About 5 h were needed for the model to integrate forward 5 min using 26 processors. Had grid 4 been initialized at 1200 UTC, a 12-h run would have required at least 720 h, or nearly 1 month. Such computational requirements demonstrate that a 32-bit single processor computer, even one with parallel computing capabilities, is inadequate for this type of research.

4. Synthetic images

During the integration of grid 4, model output was written at the GOES-R ABI temporal sampling rate of 5 min from both grid 3 (for synthetic GOES-R ABI imagery) and grid 4 (for synthetic NPOESS VIIRS imagery) for this simulation. As a result of the size of grid 3 and grid 4, about 5.5 GB of data were written at each output time. This is just under 70 GB of data per simulated hour. Output from RAMS was then used as input to the observational operator.

One of the first calculations performed by the observational operator was to compute the gaseous transmittance at a specific GOES-R ABI or NPOESS VIIRS channel. Spectral coefficients for these wavelengths specific to GOES-R ABI were obtained from the US Joint Center for Satellite Data Assimilation. As VIIRS spectral coefficients were not available, values from the MODIS Terra instrument at 8.53, 11.02 and 12.03 μm were chosen. OPTRAN (McMillin *et al.* 1995) was then used to calculate the gas transmittance based on values of temperature, water

vapour and pressure provided by RAMS. Values of ozone were also required, thus a standard climatological vertical profile was used. One consequence of this was to set the top of the RAMS domain high enough to capture the increase of ozone with height because GOES-R ABI will have a 9.61 μm band. Examination of the ozone profile showed that the maximum ozone concentration occurred near 5 hPa (mb). As neither RAMS nor the data used to initialize RAMS extended to that pressure, the ozone peak was only partially captured. Next, values of single-scattering albedo and extinction were computed for each of the seven hydrometeor types (cloud water, rain water, hail, graupel, aggregates, snow, and pristine ice) using modified anomalous diffraction theory (Mitchell 2000). A choice existed for the treatment of the asymmetry factor: either calculate this value based on anomalous diffraction theory or simply set the asymmetry to a constant value of 0.9. As brightness temperatures at wavelengths greater than 3.9 μm showed little sensitivity to the choice of how the asymmetry factor was determined, the constant value of 0.9 was chosen. However, a constant value of 0.9 for the asymmetry factor may be inappropriate for calculations of brightness temperatures at 3.9 μm. Therefore, methods are being explored to obtain more accurate values of this parameter. Bulk optical properties were then computed as a number concentration weighted mean of the individual optical properties of each hydrometeor type.

At this point in the observational operator, two different paths were chosen based on the wavelength for which brightness temperatures were computed. For the nine GOES-R ABI wavelengths greater than 3.9 μm and the three VIIRS bands, brightness temperatures were computed using the Delta-Eddington two-stream method (Deeter and Evans 1998) along with a horizontally constant surface emissivity of 0.98. Brightness temperatures at 3.9 μm were computed using a recently developed one-dimensional version (called SHDOMPP) of the Spherical Harmonic Discrete Ordinate Method (SHDOM; Evans 1998). SHDOMPP requires not only the solar zenith angle but also coefficients of the Legendre phase function. In addition, a horizontally constant value of 0.2 was chosen for the surface albedo.

In contrast to brightness temperatures at wavelengths greater than 3.9 μm, brightness temperatures at 3.9 μm were more sensitive to values of the single-scattering albedo and asymmetry factor. In particular, values of both single-scattering albedo and asymmetry factor exhibit relatively large changes for small changes in ice particle size near and below about 30 μm. In addition, the Henyey–Greenstein phase function depends on the value of the asymmetry factor. Thus brightness temperatures can exhibit relatively large variations, of the order of 5 K, for relatively small changes in optical properties. Therefore, accurate values of the phase function and single-scattering albedo are required. One approach is the use of light scattering calculations such as those provided by Yang *et al.* (2000). This approach is currently being explored. As a first step, modified anomalous diffraction theory was used to compute values of the single-scattering albedo and 0.9 was used as the value for the asymmetry factor.

Final calculations in the observational operator were the spectral radiances at a given GOES-R ABI or VIIRS wavelength. By comparison, SHDOMPP required the most time to produce one synthetic 3.9 μm image. Approximately 20 min were needed to produce one GOES-R ABI synthetic image at any wavelength larger than 3.9 μm in grid 3. Recall that this grid had $502 \times 522 \times 60$ points. When SHDOMPP was run to produce one synthetic image at 3.9 μm in the same grid, about 2 days elapsed before a complete two-dimensional spectral radiance field was produced. As

a consequence, efforts are under way to convert SHDOMPP to run in parallel in an attempt to improve computational efficiency.

Synthetic GOES-R ABI imagery was generated every 5 min over a 6-h period for the following nine wavelengths: 6.815, 6.95, 7.34, 8.5, 9.61, 10.35, 11.2, 12.3 and 13.3 μm. Synthetic NPOESS VIIRS imagery was created for one time at 8.53, 11.02 and 12.03 μm. Instead of showing an example of synthetic imagery at each wavelength, one synthetic image from GOES-R ABI and NPOESS VIIRS is shown for brevity. Figure 3(*a*) shows the synthetic 2 km GOES-R ABI image with a central wavelength of 10.35 μm. This image also contains the outline of two boxes. The larger box shows the location of the corresponding synthetic 400 m NPOESS VIIRS image that has a central wavelength of 11.02 μm (figure 3(*b*)). In this case, the size of the NPOESS image is approximately 400 km on a side, which is much smaller than the proposed swath dimensions. As can be seen, considerably more detail is contained in this image.

A synthetic 4 km GOES-12 image with a central wavelength at 10.7 μm was produced over the same domain that is covered by the synthetic GOES-R ABI image. Because of the relatively large FOVs of the synthetic GOES-12 and GOES-R images, patterns of brightness temperatures look similar between the two sensors. This is because the difference between a 2 km and a 4 km footprint is almost indistinguishable for the area covered by grid 3. As a result, a smaller region of the domains was magnified to facilitate a comparison between the two images. The thunderstorm over southeast Kansas, bounded by the smaller box in figure 3(*a*), is displayed in figure 4. This region has been magnified to the point where individual pixels can be seen. As a result, additional detail can be seen in the 2 km GOES-R ABI image (figure 4(*b*)) compared to the corresponding 4 km GOES-12 image (figure 4(*a*)). Differences between the two images are a result of (1) the smaller 2 km footprint of GOES-R ABI compared to the 4 km footprint of the operational GOES-12 Imager and (2) differences in the central wavelength and spectral width of

(*a*)   (*b*)
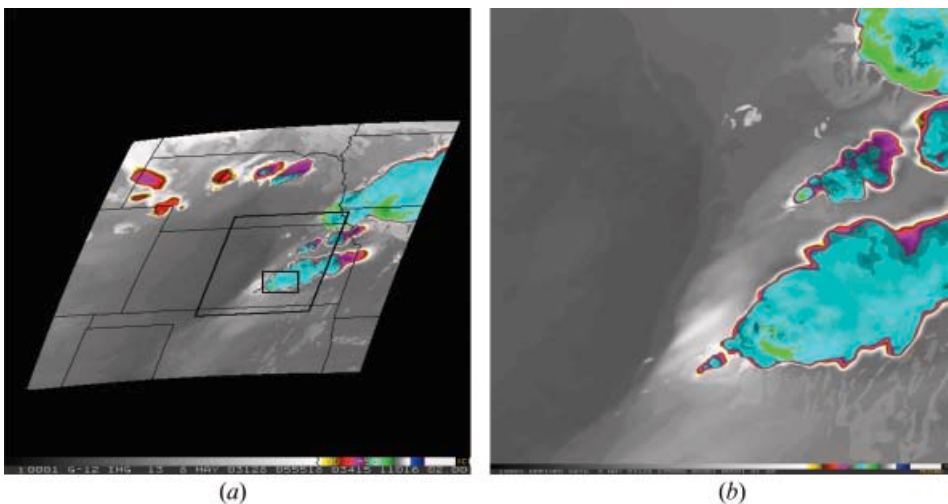
Figure 3.   (*a*) Synthetic 2 km GOES-ABI at 10.35 μm and (*b*) synthetic 400 m NPOESS VIIRS at 11.02 μm for the 8 May 2003 severe weather event at 2355 UTC. The larger box in (*a*) shows the region of the NPOESS VIIRS image while the smaller box denotes the location of the zoomed image in figure 4.
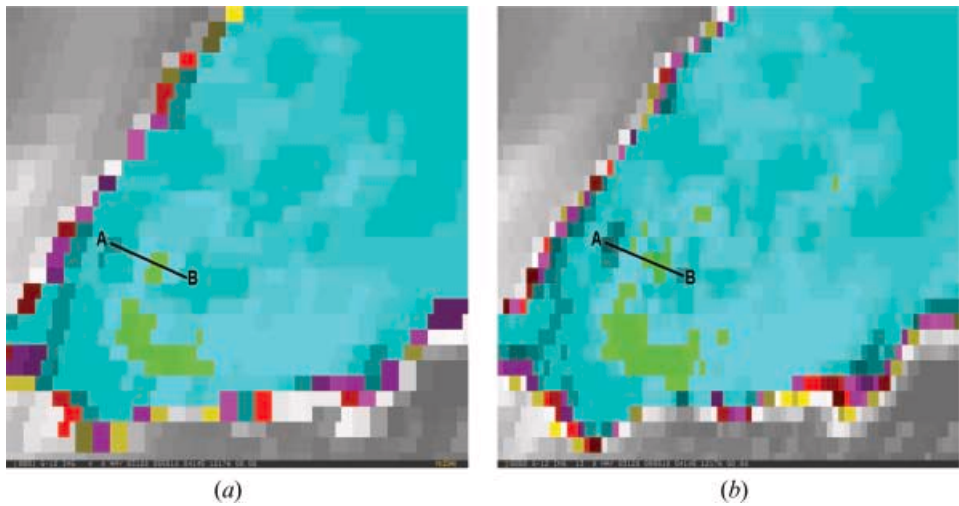
Figure 4. Magnified (*a*) synthetic 4 km GOES-12 10.7 μm image and (*b*) synthetic 2 km GOES-R 10.35 μm image of the thunderstorm over southeast Kansas depicted in figure 3.

the longwave infrared band for the GOES-12 Imager compared to that proposed for GOES-R ABI. Specifically, the central wavelength on the GOES-12 Imager is 10.7 μm and the band ranges from 10.2 μm to 11.2 μm. In comparison, the central wavelength on the ABI is 10.35 μm and the band ranges from 10.1 μm to 10.6 μm. As the footprint size decreases from that of the Imager on GOES-12 to that of the ABI on GOES-R, additional details in retrieved quantities will be realized. For example, the line from A to B in figures 4(*a*) and 4(*b*) passes through an overshooting top. Some rain rate products are based on a correlation between brightness temperatures and radar-derived rain rates. As a result, rain rates from the GOES-R image will have a greater variation, along the line from A to B, compared to rain rates from the GOES-12 image. That is, the warmer pixels located at A and B in figure 4(*b*) will have a smaller rain rate compared to those regions in figure 4(*a*). Similarly, the colder overshooting top located approximately midway on the line from A to B in figure 4(*b*) will have a larger rain rate compared to that in figure 4(*a*).

5. Discussion

Once created, the usability of synthetic GOES-R ABI and NPOESS VIIRS imagery can be explored. GOES-R ABI images can be combined to produce Derived Product Imagery (DPI). DPI is useful in the detection of several different types of events; for example, low clouds composed of liquid water, fog, and skin temperature. Cloud particle size may be retrieved with the use of imagery at 3.9 μm. Synthetic GOES-R ABI brightness temperatures at 12.3 μm can be subtracted from those at 10.35 μm for the detection of thin cirrus. In addition, synthetic GOES-R ABI and NPOESS VIIRS imagery can be used by current algorithms and then be used to aid in the development of algorithms for future environmental satellites. For example, upper tropospheric winds can be derived from imagery in the water vapour bands while synthetic GOES-R ABI imagery at 9.61 μm can be used to develop algorithms for lower stratospheric ozone.

Algorithm development to retrieve information about fires will make use of synthetic imagery at 3.9 μm and 11.2 μm. Because satellite fire detection is a current study at CIRA, this application is discussed in more detail. One goal is to show the utility of synthetic imagery for algorithm development and other issues of future sensors. As stated above, grid 4 had 400 m grid spacings in each horizontal direction over eastern Kansas (figure 2). At that location, the size of a GOES-R ABI 3.9 μm pixel will be nearly 2.4 km in the east–west direction and 3.2 km in the north–south direction. As a result, aggregates of 400 m footprints from grid 4 can be subpixel information for the ABI sensor. Thus, synthetic GOES-R ABI 3.9 μm imagery of grid 4 has been produced that contains ground fires. Some of these fires are made up of multiples of 400 m grid cells and yet remain subpixel fires for the ABI sensor. A synthetic ABI image was made from the 400 m data by use of an appropriate point spread function that was used to build each 2.4 km × 3.2 km ABI footprint. As a result of the point spread function, information outside of each ABI pixel is contained within each ABI pixel. Once completed, the synthetic 3.9 μm image will be used as input to the Agriculture Biomass Burning Algorithm (ABBA; Prins and Menzel 1992). This algorithm estimates fire temperature and size from the synthetic imagery. As the fire temperatures and sizes were prescribed when making the synthetic 3.9 μm image, ABBA-retrieved fire temperatures and sizes can be compared directly to these 'truth' values. In addition, ABI pixels will have a nearly fixed latitude and longitude associated with them. As a consequence, fire hotspots will look different depending on the location of the ground fire relative to an ABI pixel location. Synthetic imagery at 3.9 μm of fire hot spots will be used to understand how ABI sampling of fires may affect how fire signatures look in the imagery. This is just one example of the utility of synthetic imagery in aiding algorithm development. Additional results from this study will appear in a future paper.

Work is under way to generate synthetic images that contain a solar component. This includes seven proposed channels for GOES-R ABI. Synthetic imagery at 3.9 μm is currently being produced for the above case. Imagery at the first six GOES-R ABI channels 0.47, 0.64, 0.865, 1.378, 1.61 and 2.25 μm will be produced at a later time when the spectral coefficients for these bands become available. Furthermore, synthetic NPOESS imagery can be expanded into the microwave region. Data of this type can be used to diagnose the pressure, winds and intensity of tropical cyclones from synthetic brightness temperatures. In addition, such imagery can be used to evaluate sounding retrieval algorithms.

Additional motivation for using numerical models to create synthetic satellite imagery can be seen in the areas of algorithm development, numerical weather prediction verification, and the interpretation of satellite imagery. Two examples follow: first, imagery from multiple channels can be combined to aid in the detection of supercooled liquid water. This has an immediate application to aircraft safety. Second, imagery at 0.47 μm can be used to detect aerosols such as smoke from wildfires and blowing dust. Synthetic satellite imagery can also be used for numerical weather prediction verification by comparing synthetic imagery from a forecast model to observed imagery (Panegrossi *et al.* 1998, Kummerow *et al.* 2001, Chaboureau *et al.* 2002). Synthetic water vapour imagery can be used to determine how well a numerical model predicts the movement of mid-tropospheric water vapour. Finally, past studies have shown that brightness temperatures at 6.7 μm can at times be larger than those at 11 μm for thunderstorm anvils (Ackerman 1996).

The combination of forecast model output, radiative transfer model output and synthetic imagery can be used to help in understanding this observation.

6. Future directions

Future work will focus on two areas: assessment of synthetic imagery and generating synthetic 3.9 μm imagery using light scattering calculations. Validating synthetic imagery will make use of histograms. For example, one possible procedure could be to define a temperature threshold that will isolate thunderstorm anvils in not only synthetic GOES-12 imagery but also actual GOES-12 imagery. Statistical methods can then be used to calculate metrics such as the mean and standard deviation of both data sets. This will allow for identification of any biases in the synthetic imagery. The second topic, generating synthetic 3.9 μm images, will focus on using light scattering calculations. Such calculations will be used to obtain Legendre coefficients in place of those calculated from the Henyey–Greenstein approximation. In addition, this procedure will provide optical properties that will replace those computed using modified anomalous diffraction theory. Both of these topics will be discussed in detail in forthcoming papers.

7. Summary

Both GOES-R ABI and NPOESS VIIRS are planned to be in orbit in 2012. Efforts are under way to obtain simulated and synthetic imagery for both satellites. Current operational and research satellite images are being used to simulate imagery for these two future sensors. Numerical models have also been used to create synthetic imagery for these two sensors. The potential use of both simulated and synthetic imagery is many-fold and applies to any international environmental satellite sensor.

The 8 May 2003 severe weather event over mid-western USA was simulated with the RAMS mesoscale model. Output from this model was used as input to an observational operator. This model is used to produce synthetic imagery at a specific wavelength for a specific sensor. Synthetic GOES-12, GOES-R ABI and NPOESS VIIRS imagery was created for this case. Generating GOES-12 synthetic imagery allowed for easy comparison between a current operational sensor and a future sensor. By magnifying the synthetic images from both GOES-12 and GOES-R ABI, differences in the imagery were detected between the two sensors.

B simulated and synthetic imagery have many uses. Synthetic imagery, in particular, can be tested by current operational algorithms to derive, for example, water vapour winds and hot spot locations associated with fires. This type of imagery can also be used to aid in the development of algorithms for the future sensors. Future work will concentrate on validation of synthetic GOES-R ABI imagery. Furthermore, generating synthetic 3.9 μm will be explored using light scattering calculations.

References

ACKERMAN, S.A., 1996, Global satellite observations of negative brightness temperature differences between 11 and 6.7 μm. *Journal of the Atmospheric Sciences*, **53**, pp. 2803–2812.

AUMANN, H.H., CHAHINE, M.T., GAUTIER, G., GOLDBERG, M.D., KALNAY, E., MCMILLIN, L.M., REVERCOMB, H., ROSENKRANZ, P.W., SMITH, W.L., STAELIN, D.H., STROW, L.L. and SUSSKIND, J., 2003, AIRS/AMSU/HSB on the aqua mission: design, science objectives, data products, and processing systems. *IEEE Transactions on Geoscience and Remote Sensing*, **41**, pp. 253–264.

CHABOUREAU, J.-P., CAMMAS, J.-P., MASCART, P. and PINTY, J.-P., 2002, Mesoscale model cloud scheme assessment using satellite observations. *Journal of Geophysical Research*, **107**(D16), pp. 4301.

CHABOUREAU, J.-P. and PINTY, J.-P., 2006, Evaluation of a cirrus parameterization with Metoesat Second Generation. *Geophysical Research Letters*, **33**, pp. L03815.

CHEVALLIER, F., BAUER, P., KELLY, G., JAKOB, C. and MCNALLY, T., 2001, Model clouds over oceans as seen from space: comparison with HIRS/2 and MSU radiances. *Journal of Climate*, **14**, pp. 4216–4229.

CHEVALLIER, F. and KELLY, G., 2002, Model clouds as seen from space: comparison with geostationary imagery in the 11-μm window channel. *Monthly Weather Review*, **130**, pp. 712–722.

COTTON, W.R., PIELKE, R.A., Sr., WALKO, R.L., LISTON, G.E., TREMBACK, C.J., JIANG, H., MCANELLY, R.L., HARRINGTON, J.Y., NICHOLLS, M.E., CARRIO, G.G. and MCFADDEN, J.P., 2003, RAMS 2001: current status and future direction. *Meteorology and Atmospheric Physics*, **82**, pp. 5–29.

DEETER, M. and EVANS, K.F., 1998, A hybrid Eddington single-scatter radiative transfer model for computing radiances from thermally emitting atmospheres. *Journal of Quantitative Spectroscopy and Radiative Transfer*, **60**, pp. 635–648.

EVANS, K.F., 1998, The spherical harmonics discrete ordinate method for three-dimensional atmospheric radiation transfer. *Journal of the Atmospheric Sciences*, **55**, pp. 429–446.

GRASSO, L.D. and GREENWALD, T., 2004, Analysis of 10.7 μm brightness temperatures of a simulated thunderstorm with two-moment microphysics. *Monthly Weather Review*, **132**, pp. 815–825.

GREENWALD, T.J., HERTENSTEIN, R. and VUKICEVIC, T., 2002, An all-weather observational operator for radiance data assimilation with mesoscale forecast models. *Monthly Weather Review*, **130**, pp. 1882–1897.

HILLGER, D.W. and CLARK, J.D., 2002, Principal component image analysis of MODIS for volcanic ash. Part I: Most important bands and implications for future GOES imagers. *Journal of Applied Meteorology*, **41**, pp. 985–1001.

KING, M.D., KAUFMAN, Y.J., MENZEL, W.P. and TANRE, D., 1992, Remote sensing of cloud, aerosol and water vapor properties from the Moderate Resolution Imaging Spectroradiometer (MODIS). *IEEE Transactions on Geoscience and Remote Sensing*, **30**, pp. 2–27.

KUMMEROW, C., HONG, Y., OLSON, W.S., YANG, S., ADLER, R.F., MCCOLLUM, J., FERRARO, R., PETTY, G., SHIN, D.-B. and WILHEIT, T.T., 2001, The evolution of the Goddard Profiling Algorithm (GPROF) for rainfall estimation from passive microwave sensors. *Journal of Applied Meteorology*, **40**, pp. 1801–1820.

LI, J., MENZEL, W.P., ZHANG, W.J., SUN, F.Y., SCHMIT, T.J., GURKA, J.J. and WEISZ, E., 2004, Synergistic use of MODIS and AIRS in a variational retrieval of cloud parameters. *Journal of Applied Meteorology*, **43**, pp. 1619–1634.

MCMILLIN, L.M., CRONE, L.J., GOLDBERG, M.D. and KLEESPIES, T.J., 1995, Atmospheric transmittance of an absorbing gas. 4. OPTRAN: a computationally fast and accurate transmittance model for absorbing gases with fixed and variable mixing ratios at variable viewing angles. *Applied Optics*, **34**, pp. 6269–6274.

MILLER, S.D., HAWKINS, J.D., KENT, J., TURK, F.J., LEE, T.F., KUCIAUSKAS, A.P., RICHARDSON, K., WADE, R. and HOFFMAN, C., 2006, Nexsat previewing NPOESS/ VIIRS imagery capabilities. *Bulletin of the American Meteorological Society*, **87**, pp. 433–446.

MITCHELL, D.L., 2000, Parameterization of the Mie extinction and absorption coefficients for water clouds. *Journal of the Atmospheric Sciences*, **57**, pp. 1311–1326.

MORCRETTE, J.-J., 1991, Evaluation of model-generated cloudiness: satellite-observed and model-generated diurnal variability of brightness temperatures. *Monthly Weather Review*, **119**, pp. 1205–1224.

PANEGROSSI, G., DIETRICH, S., MARZANO, F.S., MUGNAI, A., SMITH, E.A., XIANG, X.W., TRIPOLI, G.J., WANG, P.K. and BAPTISTA, J.P.V.P., 1998, Use of cloud model microphysics for passive microwave-based precipitation retrieval: significance of consistency between model and measurement manifolds. *Journal of the Atmospheric Sciences*, **55**, pp. 1644–1673.

PRINS, E.M. and MENZEL, W.P., 1992, Geostationary satellite detection of biomass burning in South America. *International Journal of Remote Sensing*, **13**, pp. 2783–2799.

RAYMOND, W.H. and AUNE, R.M., 2003, Conservations of moisture in a hybrid Kuo-type cumulus parameterization. *Monthly Weather Review*, **131**, pp. 771–779.

SCHMIT, T.J., GUNSHOR, M.M., PAUL MENZEL, W., LI, J., BACHMEIER, S. and GURKA, J., 2005, Introducing the next-generation advanced baseline imager (ABI) on Geostationary Operational Environmental Satellites (GOES)-R. *Bulletin of the American Meteorological Society*, **86**, pp. 1079–1096.

YANG, P., LIOU, K.N., WYSER, K. and MITCHELL, D., 2000, Parameterization of the scattering and absorption properties of individual ice crystals. *Journal of Geophysical Research*, **105**, pp. 4699–4718.